INVESTIGATION OF THE FLOW OVER NACELLE/PYLON AND WING CONTROLLED WITH A VORTEX GENERATOR IN HIGH-LIFT CONFIGURATION

Yuzuru YOKOKAWA*, Masahiro KANAZAKI, Mitsuhiro MURAYAMA***
Hiroyuki KATO*, Takeshi ITO*, Kazuomi YAMAMOTO*
***Japan Aerospace Exploration Agency**
****Tokyo Metropolitan University**

Keywords: *high-lift, vortex, Kriging model, chine, PIV*

Abstract

Aerodynamic performance near maximum lift condition of high-lift configuration commercial aircraft model was improved by a kind of vortex generator "chine" installed on the nacelle in lowspeed wind tunnel testing. At first, interference between a nacelle and a main-wing was observed using experimental and also computational results. Then, the optimum location for the chine is explored applying an efficient design process using Generic Algorism (GA) with Kriging surrogate model in the experiment. Results of PIV measurement have clarified how the longitudinal vortex from the chine controls separated flow field structure near the nacelle/pylon and slat-cutoff region.

1 Introduction

Accurate prediction of the maximum lift coefficient (CL_{max}), lift/drag (L/D) ratio and their Reynolds number dependency for high-lift configuration is essential issues for an aerodynamic design because successful improvement has a strong impact on the whole performance of an aircraft. They are most challenging task, because flow features on multi elements wing configuration include many kinds of boundary layer transition, separations, interactions, and also 3D behavior, as well as its complicated geometry. In the European research project EUROLIFT, collaborative work together with a lot of research institutes for the development of high-lift system design technology has been extensively performed with both experiment and computation up to flight Reynolds number[1-8]. In the report[6,7], it is mentioned that interaction between an engine-nacelle and a wing was one of the principal reasons for Reynolds number effect of the maximum lift coefficient.

In Japan Aerospace Exploration Agency (JAXA), a research program to make design methodology for advanced high-lift system has been performed[9,10]. As the step of the program, lowspeed wind tunnel testing campaign using a realistic aircraft configuration model with leading-edge slat, flaps, fuselage and nacelle-pylon was implemented through 2005 to 2007. In the testing, we focused our attention to acquiring both precise validation data for CFD and detailed flow information for a prediction of lift performance in actual aircraft configuration[11-13]. In our research also, serious interaction between the long-cowling type nacelle and a wing causes adverse Reynolds number effect, which appeared in the force measurement and surface flow visualizations[11,12].

In this paper, we initially understand basic aerodynamics and installation effect of the two kinds of nacelles. Following that, stall performances is improved by the vortex generator called "chine" installed on nacelle. The effective way to explore an optimum location for aerodynamic device applying the design exploration with Genetic Algorithm (GA) is used. The purpose of this paper is to clarify the behavior of the vortex from the chine and its interaction with original flow field on a nacelle, a pylon and a wing.

2 Experimental Method

2.1 High-lift Configuration Wing Model

"JSM (JAXA high-lift configuration Standard Model)" is a generic high-lift configuration aircraft model which assumes a modern and typical 100-passenger class regional jet airliner. To maximize Reynolds number based on the mean aerodynamic chord (MAC), the model is a half-span type. As shown in Fig.1 we equipped the model with a circular fuselage and a flow through nacelle/pylon at under the wing and three Flap Track Fairings (FTF) as well as high-lift devices, so that the model can provide detailed flow fields occurring in actual aircraft. The model geometries are 2.3m in the half wing span, 4.9m in the fuselage length, 0.5m in the fuselage diameter, which is about 17% similarity of the assumed aircraft. The wing has 9.42 of the aspect ratio and 33degrees of the leading-edge sweep angle.

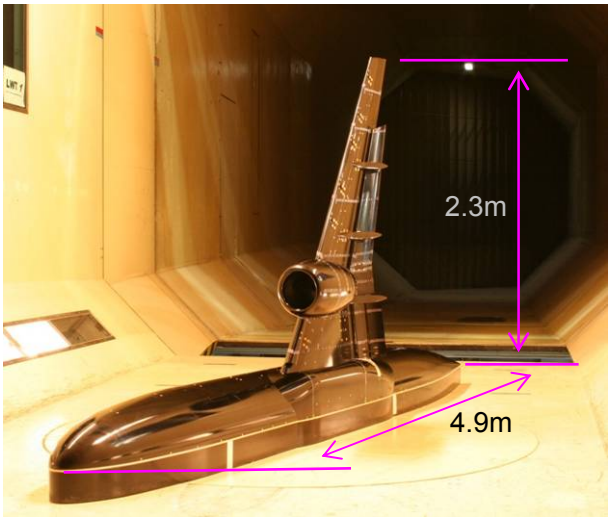

Figure 1. JSM in JAXA-LWT1 test section.

The extent of the leading-edge slat is 85% of semi-span length and the chord length is 12% of stowed wing chord length, which is supported by eight slat tracks. The flap is 77% of semi-span length and 30% of stowed wing chord length. There are double-slotted flap at the inboard (up to 37%) and a single-slotted flap at the outboard (up to 77%), as shown in Fig. 1. In this paper, only results for the landing phase are shown, where the high-lift devices are deflected in 25deg for the slat, 35deg for the flap and 20deg for the aft-flap. In order to observe aerodynamic interference between a nacelle/pylon and a wing, this model can select nacelle shape from either a long-cowling type or a short-cowling with a core type. They are presented in Fig.2. The model has total of 456 static pressure taps at seven cross sections on the wing, four cross sections on the fuselage and also on the nacelle-pylon.

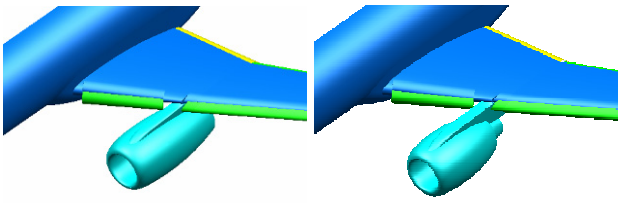

Figure 2. Two type of the nacelles.
(left: Long-cowling, right: Short-cowling)

2.2 Facility and Experimental Apparatus

The wind tunnel facility used in this testing is 6.5m by 5.5m Lowspeed Wind Tunnel in JAXA (JAXA-LWT1), which is an atmospheric pressure closed-circuit tunnel with an octagonal cross section. A maximum flow speed at the test section is up to 70*m/s*. In the case of our testing with JSM, Reynolds number based on MAC is up to about 2.5million. The model was mounted vertically on the turntable for changing an angle of attack (AoA). To avoid interference between the model and the boundary layer of the tunnel wall, a spacer with 150mm height was set below the fuselage. Under the model, five components moment-type balance was installed to measure two elements of forces and three elements of moments. The accuracy of the balance is about 0.01 and 10 counts in lift and drag coefficient, respectively, which is sufficient level in the aerodynamic testing for high lift devices[14]. The surface pressure distribution was measured with electronic pressure scanners mounted inside the model. Surface flow pattern was visualized by the fluorescent oil-flow method and images were taken by digital cameras and digital video camera during or after the wind tunnel running.

As shown in Fig. 3, three-dimensional flow field was acquired by stereoscopic PIV measurement[15]. The PIV system mainly

consists of a high-power laser, two CCD cameras, PIV software (LaVision, DaVis7), a stereo calibration target with a micro adjustment traverse system, and optical components including laser light sheet optics. The laser is a two cavity double-pulse Nd:YAG laser with maximum pulse energy of 200 mJ/pulse at a repetition rate of 10 Hz. The cameras are 14-bit monochrome unintensified cross-correlation CCD cameras with 2048 x 2048 pixels, which obtain three-component velocity vector maps at around 2 Hz.

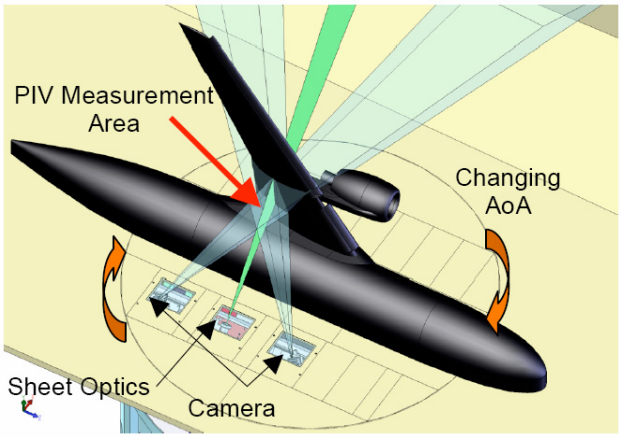

Figure 3. Stereoscopic PIV setting.[15]

As shown in Fig.3, a traverse system for both cameras in stereoscopic view and the laser with the light sheet optics was devised to guide the laser beam through the optical window of the wind tunnel turntable. Using this traverse system, the measurement planes were always kept perpendicular to the model fuselage axis with changing angle of attack. In this measurement, three components of velocity field were measured in each cross flow plane along the model fuselage axis on the upper side of the wing.

3 Results and Discussions

3.1 Basic Aerodynamics

In this section, basic aerodynamics obtained in the wind tunnel testing for both the long- and the short-cowling nacelles are presented. In the measurement, the data were acquired in pitch pause mode as the angle of attack was increasing. All data were provided after correction of the tunnel wall and other interference by the method given by Alan Pope[16]. Results of Navier-Stokes computations performed on unstructured hybrid mesh[9,10,13] were used for better under standing of the experimental phenomena.

3.1.1 Long-cowling nacelle configuration

Figure 4 shows the change in lift coefficients with angle of attack for the long-cowling nacelle configuration at freestream velocity V = 30*m/s*, 40*m/s*, 50*m/s* and 60*m/s*. In the figure, computational result for 60*m/s* case is shown with filled dots. Lift curves of the experimental results have two remarkable aspects. In linear range within AoA=0 to 10deg, typical Reynolds number dependency is observed, where lift curves which have almost the same gradient move upward as freestream velocity increases. On the contrary to that, the other feature is visible in the stall region. Lift performance nearby the stall strongly depends on the freestream velocity condition. For 60*m/s*, stall occurs and lift drops away rapidly at AoA=12deg. Lift curve for 30*m/s* has the highest maximum lift coefficient and the stall angle of attack among four. Slow progress of the stall region is indicated because the stall occurs not immediately after the linear range but after the lift increment with lower gradient. At 40*m/s* and 50*m/s*, intermittent characters between 30*m/s* and 60*m/s* are found. The lift curves have second peak after the stall angle of attack, which is the same as that of 30*m/s*. In conclusion, the magnitude of the maximum lift coefficient and stall angle of attack tends to increase with the decrease of freestream velocity. This is the inverse phenomenon against the typical Reynolds number effect appearing in the linear region. Ordinary, the phenomenon tends to appear at higher Reynolds number about 10million or more[17,18], which is caused by a trade-off between the transition and the separation on the wing. However results shown in Fig.4 occurs lower Reynolds number at most 2.5million. Comparison of the lift coefficient with computational results shows good agreement before the stall. The value and the gradient in linear region have slight

differences, but it could capture the whole characteristics, the stall angle of attack and the rapid dropping after the stall.

Figure 5 shows the results of oil-flow visualizations on the upper surface of the wing for $V = 60m/s$ at post-stall angle of attack 15deg. This figure can give the essential characteristics of the flow in this nacelle configuration. As shown in the picture, large separation occurs after the nacelle/pylon and slat-cutoff region. Our previous work showed that this was induced by the interaction between the wing and the nacelle/pylon[19,20]. This feature is shown in more detail in the following section.

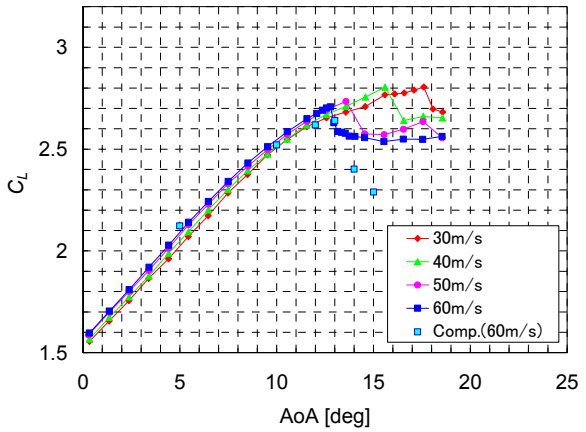

Figure 4. Lift coefficient for the long-cowling nacelle.

Figure 5. Surface flow pattern at post-stall conditions for the long-cowling nacelle. ($V = 60$m/s, AoA=15deg)

3.1.2 Short-cowling nacelle configuration

Figure 6 shows the change in lift coefficients with angle of attack for the short-cowling nacelle configuration at freestream velocity $V = 30m/s$, $40m/s$, $50m/s$ and $60m/s$. Computational result for $60m/s$ case is shown with filled dots also in this figure. Lift performance after linear range for this configuration is shown to be different from the long-cowling nacelle configuration. In this case, typical Reynolds number dependency is observed in both linear and stall region through 30 *m/s* to 60 *m/s*. Maximum lift, stall angle of attack and the reduction of the lift after the stall seem almost the same among each of cases. Because the stall occurs not immediately just after the linear range, it is possibly expected that the progress of small stall region and large separation occurs simultaneously. Lift coefficient given by computation agrees only in lower angle of attack for this configuration. The magnitude of lift coefficient after linear region can not be evaluated correctly while the gradient in linear region and stall angel of attack are comparatively similar to experimental result.

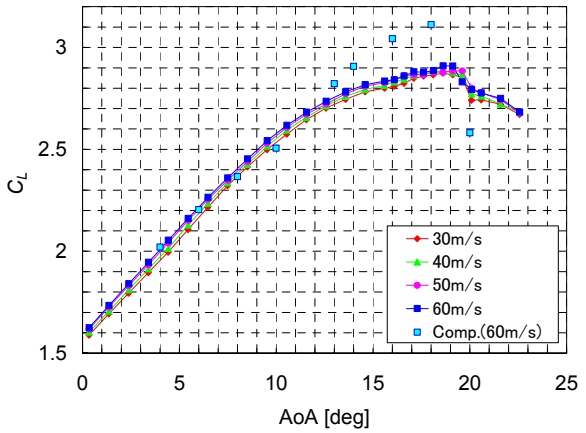

Figure 6. Lift coefficient for the short-cowling nacelle.

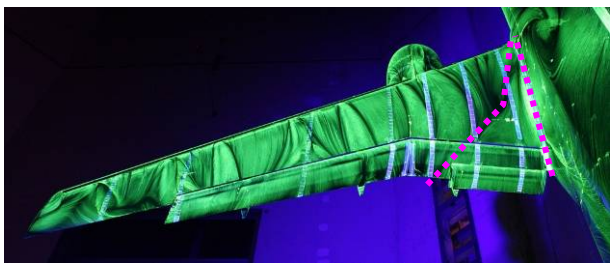

Figure 7. Surface flow pattern at post-stall conditions for the short-cowling nacelle. ($V = 60$m/s, AoA=21deg)

Figure 7 shows the results of oil-flow visualization on the upper surface of the wing for $60m/s$ at the post-stall angle of attack 21deg. Compared to the result for the long-cowling nacelle configuration shown in Fig.5, this figure shows the different stall characteristics. Large scale separation which governs the stall performance of this model occurs at the wing-root. Large separation after the nacelle-pylon and slat-cutoff region is also visible but behavior is not so serious as to lead whole of the wing to stall.

3.2 Detail observation of flow fields for each nacelle configurations

3.2.1 Nacelle installation and Reynolds Number effect on Maximum lift

As mentioned in the previous section, Reynolds number effect on maximum lift coefficient and the stall angle of attack varies depending on the nacelle configurations. Figure 8 summarizes the relation between magnitude of the maximum lift coefficient and Reynolds number. In the graph, experimental results for the model configuration removing the nacelle, where the slat is continuous and without cutoff at the pylon, is also overlapped as the reference information for a nacelle installation effect.

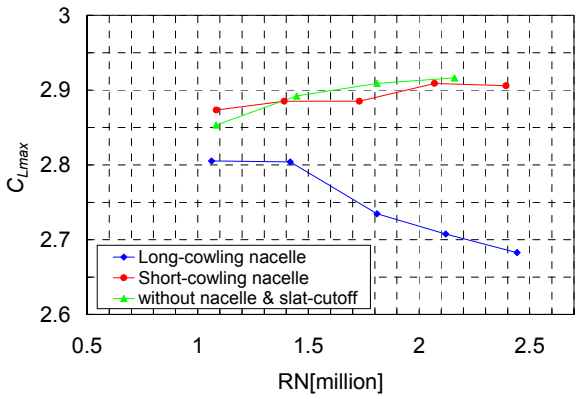

Figure 8. CL_{max} versus Reynolds number.

Based on the nacelle-OFF configuration, the installation of the long-cowling nacelle has great impact on the performance. This is caused by Reynolds number effect of the flow field on the nacelle itself or the interaction between the nacelle/pylon and the wing, as mentioned in previous sections. On the contrary to that, installation of the short-cowling nacelle does not affect the wing performance. From the maximum lift point of view, the characteristics are very similar to results of the nacelle-OFF configuration.

3.2.2 Nacelle flow field

Flow field mechanism nearby the short-cowling nacelle is assessed in detail. Figure 9 shows the results of oil-flow visualization nearby the pylon and the slat-cutoff region before and after the stall. Looking at the inboard side of nacelle, footprint of the longitudinal vortex initiation (indicated by yellow dotted-line in the figure) is found in each of the results. At the opposite side, separation line (indicated by pink dotted-line in the figure) is visible. As the separation location forwards after the stall, it is not so large. Difference from the long-cowling nacelle configuration is further visible in computational results as shown in the next figure. Figure 10 compares the three dimensional path-lines computed for each of the nacelle configuration at the post-stall angles of attack. In the figures of the long-cowling nacelle, flow passes over the inner side edge of the outboard slat, which is essential phenomenon for the stall in the case of the long-cowling nacelle configuration. However, it does not occur in the short-cowling nacelle case. The path-lines from the outboard side of the nacelle do not separate even though at the post-stall.

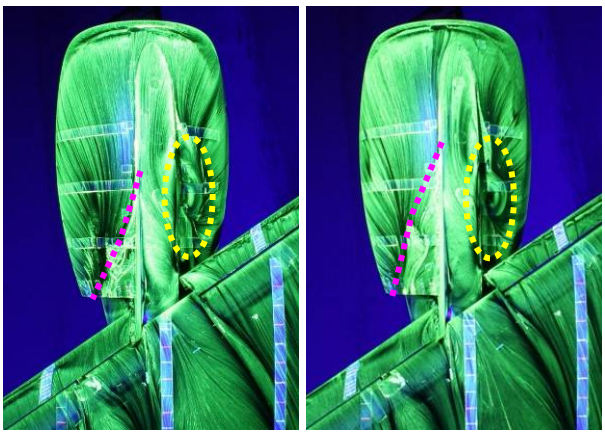

Figure 9. Surface flow pattern of the nacelle/pylon region. (AoA=18 is pre-stall, AoA=21deg is post-stall)

Throughout the consideration with experimental and computational results, it was shown that proper placement of a nacelle and a wing can reduce the serious aerodynamic interference and early stall which includes peculiar Reynolds number effect. However, even in such a configuration, flow coming from the inboard side of a nacelle is probably disturbed and it reduces the performance of the wing. It is in the "tradeoff" relation with separation from a wing-fuselage junction. In EUROLIFT project, combination of the separations between the trailing-edge of the wing-fuselage junction and the slat near inboard side of the nacelle was expected[7] up to flight Reynolds number.

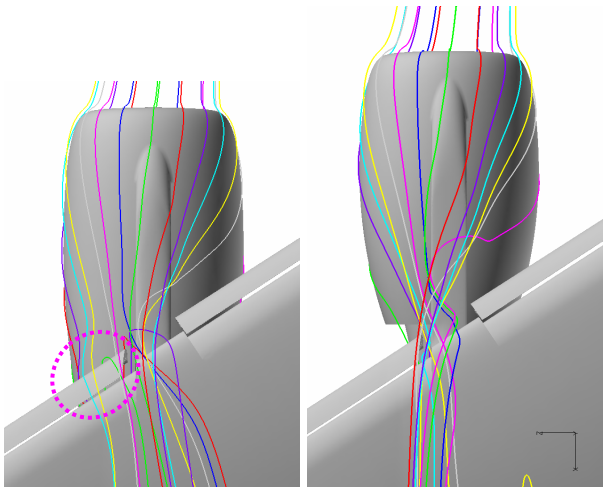

Figure 10. Path-lines near the nacelle/pylon and the wing at post-stall by computation.

3.3 Improvement of stall performance using nacelle chine

Stall performance is improved with a kind of vortex generator installed on the nacelle, which is called "chine". Flow field structure on a nacelle/pylon and a wing controlled by the chine and its vortex is observed in detail. And also, development of the methodology for an efficient position exploration in experiment was one of the main purposes in our testing because utilizing CFD to find optimum location for attaching such a small device is not realistic.

3.3.1 Effect of nacelle-chine

As the exploration methodology for the chine position, Efficient Global Optimization (EGO) with Genetic Algorithm (GA) was proposed. To reduce the evaluation cost in consideration of the wind tunnel test results, the Kriging surrogate model was introduced in EGO process. In the EGO, expected improvement (EI) [21,22] values were used as a criterion to select additional sample points. This method makes it possible not only to improve the accuracy of the surrogate model but also to explore the global optimum efficiently. More information of the methodology and consideration of the results in detail are given by Kanazaki *et al*[23]. The chine was tried to use for model configuration with the short-cowling nacelle. As shown in Fig.11, design parameters are χ and θ, which are longitudinal direction and azimuthally direction of the nacelle. Each design variable is limited as follows (Trailing edge of the chine is placed):

$$0.4C_{nacelle} \leq \chi \leq 0.8C_{nacelle}$$
$$30\ (\text{deg.}) \leq \theta \leq 90\ (\text{deg.})$$

The objective function considered here is maximum lift coefficient. In the testing, combination of the chine installation at one location and following measurement of CL_{max} were iterated according to the result based on EGO[23]. Figure 12 shows installation of the chine at two different sample locations in the experiment.

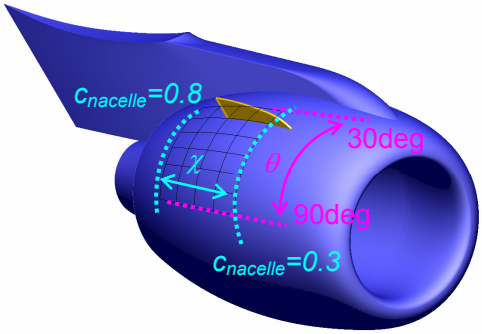

Figure 11. Installation area for the nacelle-chine.

Figure 12. Chine installation in the experiment.

After the measurements for seventeen sample installation points for V = 60m/s, the Kriging model of CL_{max} has been constructed as shown in Fig.13. (At first 10 sample points represented in red dot were used. Then, to explore better solutions based on the EI maximization, 7 samples represented in blue were added) Looking at this picture, the installation point where CL_{max} increases or decreases can be understood easily. Red area represents the location where the maximum lift is predicted to increase if the chine is installed.

Figure 14 shows the change in lift coefficients for six different locations of the chine at V = 60m/s. When the chine was installed at point_A, point_B and point_F, it has remarkably improved the lift performance from AoA=13deg then increased maximum lift

coefficients compared to the baseline configuration. Three significant information could be obtained in the results. 1) The chine makes the aerodynamic effect only beyond the linear range of lift curve otherwise it was not harmful. 2) It does not affect only maximum lift point but also recovers the end of linear range, as a result increases magnitude of maximum lift. These two aspects are reported also in EUROLIFT program[3,6]. However, in this testing, negative effect of the chine also appeared. 3) When the chine was installed point_C or point_D the lift performance was reduced rather than improved. Throughout the testing, development of methodology for efficient position exploration in the experiment has been obtained.

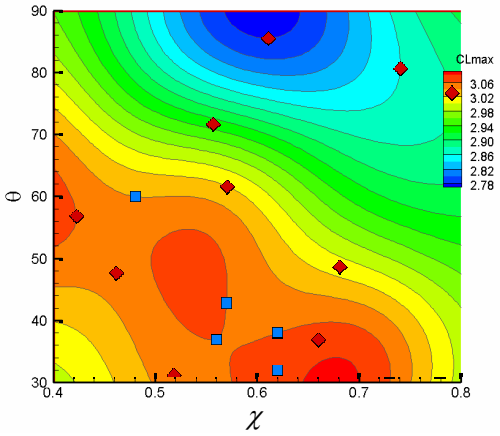

Figure 13. CL_{max} plots predicted by Kriging model.

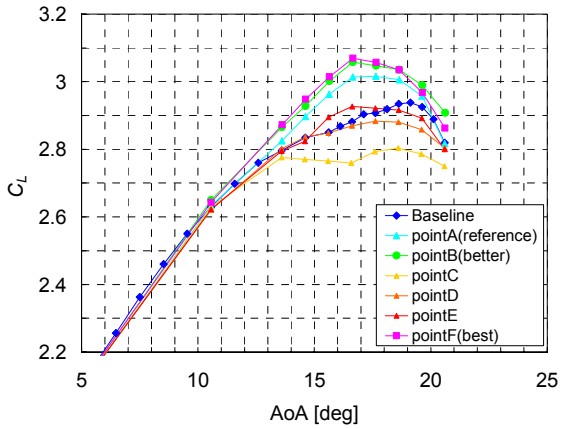

Figure 14. Effects of the nacelle-chine installation.

3.3.2 Investigation of the controlled flow field

The paper given by EUROLIFT II[7] discusses about the flow field mechanism in the case of using the aerodynamic devices on nacelle by a lot of computational and experimental results for one installation location. In our testing, vortex dynamics for three kinds of installation location, which give different performances, were investigated by PIV[15] in order to know efficient control mechanism of the disturbed flow downstream of the nacelle.

Figure 15 illustrates the effective locations for the chine installation provided by the previous exploration. Three installation points indicated in the figure were selected for PIV measurement. Their locations are as follows.

Point_F (best) : χ=0.66, θ=36.95deg
Point_B (better) : χ=0.42, θ=56.92deg
Point_C (reference): χ=0.57, θ=61.65deg

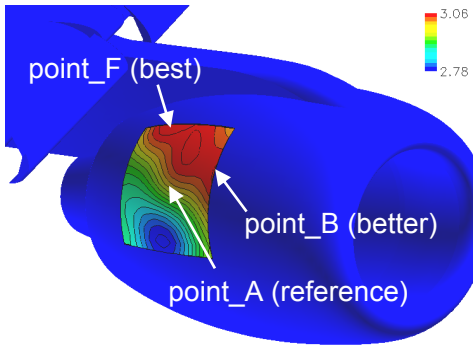

Figure 15. Response surface of CL_{max} projected on the nacelle surface

Figure 16 shows the contour map of velocity (left row) and vorticity (rigth row) magnitude at five cross sections of inboard area at AoA=16deg. Fig.16(a) is the results without the chine. On the other hand, Fig.16(b), (c), (d) is the results with the chine which is installed at point_F or point_B or point_A, respectively (They are the best, better and one more reference position in Fig.14). Freestream velocity value of 60*m/s* is subtracted from the data shown in the figure of velocity magnitude.

In Fig.16(a), loss in velocity magnitude in downstream region of the nacelle is observed. Disturbed flow which comes from the nacelle/pylon makes longitudinal vortex (pylon-vortex) and then it separates just after the slat-cutoff region. This mechanism reduces lift performance at higher angle of attack condition even though the flow separation at this location is not main reason of the stall as described 3.1.2. On the other hand, when the chine is used

installing at point_F, the other vortex with the same rotating direction which is generated by the chine (chine-vortex) appears crossing on the pylon-vortex as shown in Fig.16(b). This vortex seems to reduce the vorticity of the pylon-vortex and lowered the lowspeed region close to the surface.

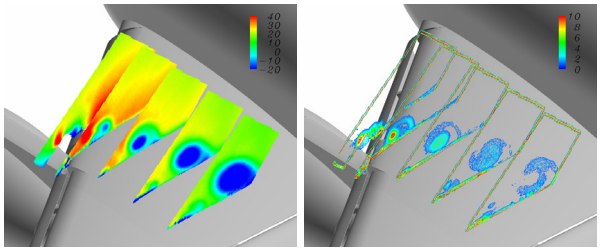

(a) Without chine

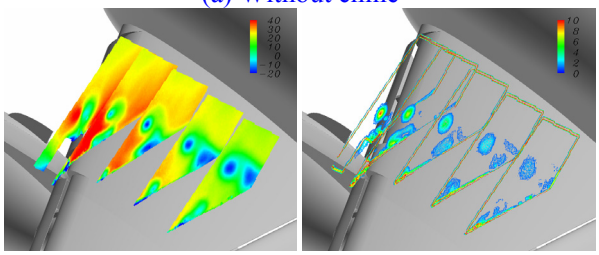

(b) Chine is installed at point_F(best)

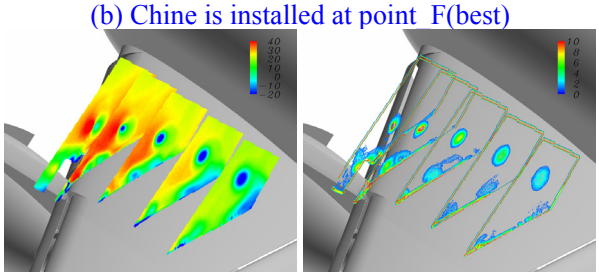

(c) Chine is installed at point_B(better)

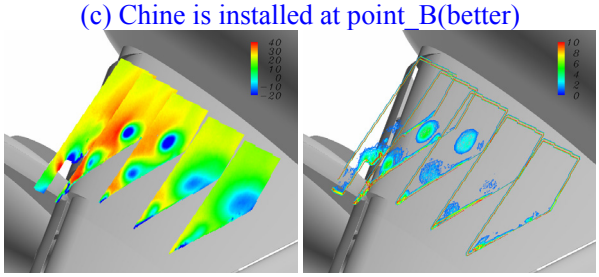

(d) Chine is installed at point_A(reference)

Figure 16. Comparison of the velocity (left row) and vorticity (right row) magnitude measured by PIV.

In the case point_B is selected, different flow structure is visible as shown in Fig.16(c), although similar effect on the lift performance to point_F can be obtained as shown in Fig.14. The chine-vortex looks stronger than that of point_F and located at the inboard side. Two vortices do not cross each other but chine-vortex seems to reduce the vorticity of the pylon-vortex and lowered the lowspeed region close to the surface also in this case.

On the contrary to that, when the chine was installed at point_A, although the chine-vortex seems to be generated in the same way, its magnitude decreases suddenly before it reaches middle chord region without interacting with the pylon-vortex as shown Fig.16(d). Consequently, loss in velocity magnitude is visible at downstream region. This feature is similar to the result of the case without chine. Obviously, lift performance with the chine at point_A is lower than that of point_F or point_B.

Now, velocity vector field acquired by PIV is observed in order to understand the origination of the vortex from the nacelle/pylon and the chine. Figure 17 shows the result for the first two sections in Fig.16 from upstream. Left row is the first section which crosses the pylon and right row is the second section. In the figure, vector is colored by the velocity magnitude (red/blue represents faster/slower than freestream velocity).

At first, when the chine is not installed, the pylon-vortex is visible above the pylon at the first section as shown in Fig.17(a). This vortex induces the upwash flow near the edge of inner slat, and then lowspeed flow region is moved upwards, which is visible at the second section. At downstream, lowspeed flow region merges with the vortex core.

On the other hand, in the case where the chine is installed at point_F, the vortex is not shown at the pylon. Only a vortex from the chine appears as shown in Fig.17(b). In this case lowspeed flow region is not moved upwards because there is no upwash flow which would be induced by the pylon-vortex, and also the chine-vortex can't make upwash just below itself. This mechanism makes it possible that lowspeed region is suppressed near the surface. It moves spanwise direction due to the induced flow by the chine-vortex that makes velocity component only in this direction. This is the reason for the crossing of two vortices in Fig16(b). It should be noted that disappearance of the pylon-vortex is not obtained by an interaction with the chine-vortex. Instead, installation of the chine changes the original flow field on the nacelle and around the pylon, and then reduces disturbed flow which goes onto the wing.

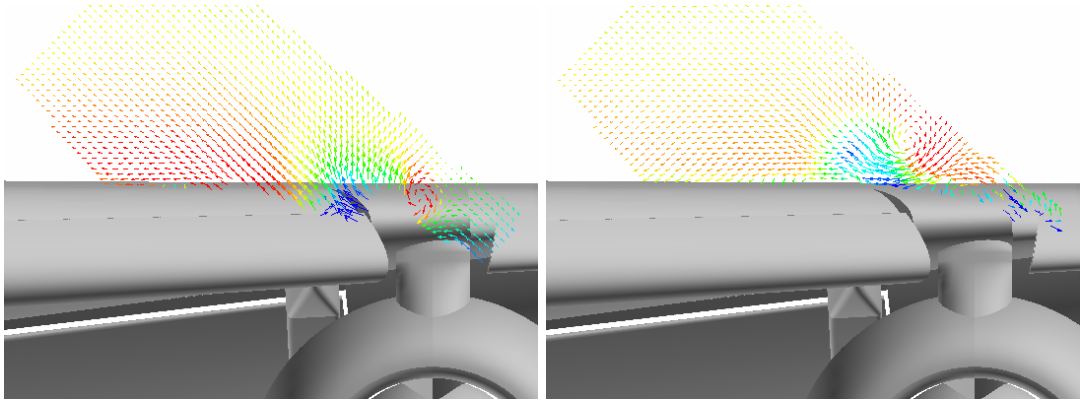

(a) Without chine

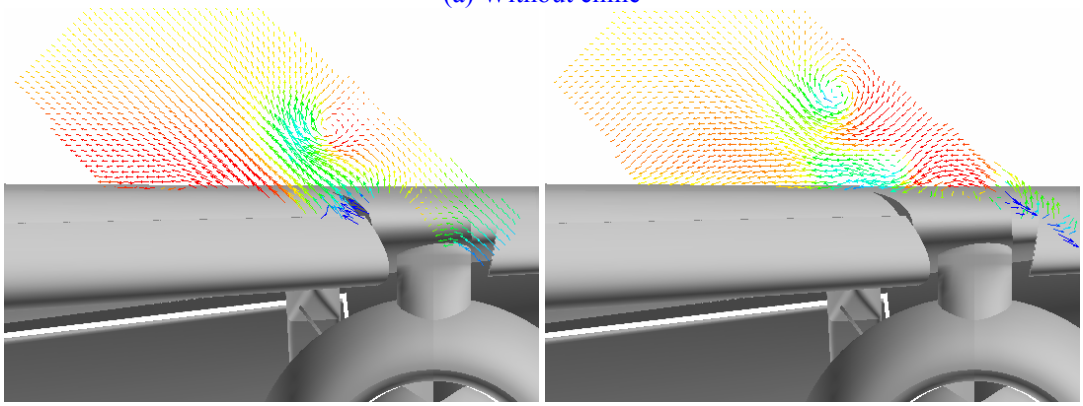

(b) Chine is installed at point_F(best)

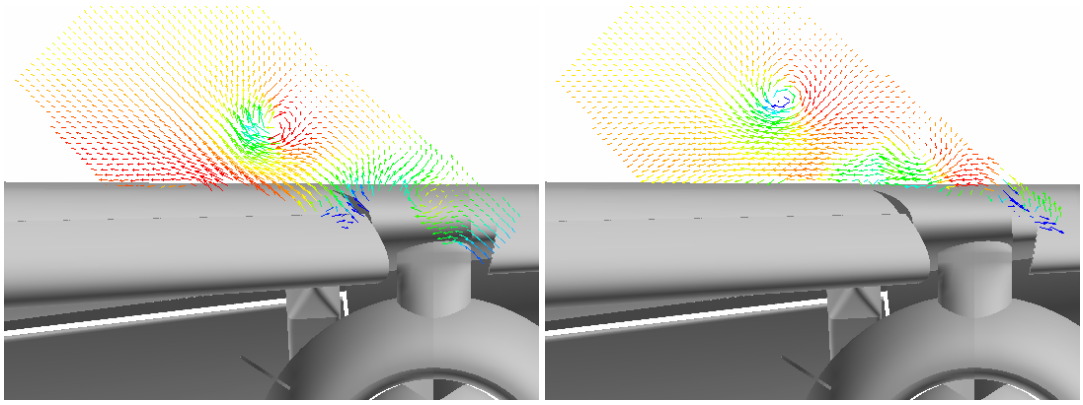

(c) Chine is installed at point_B(better)

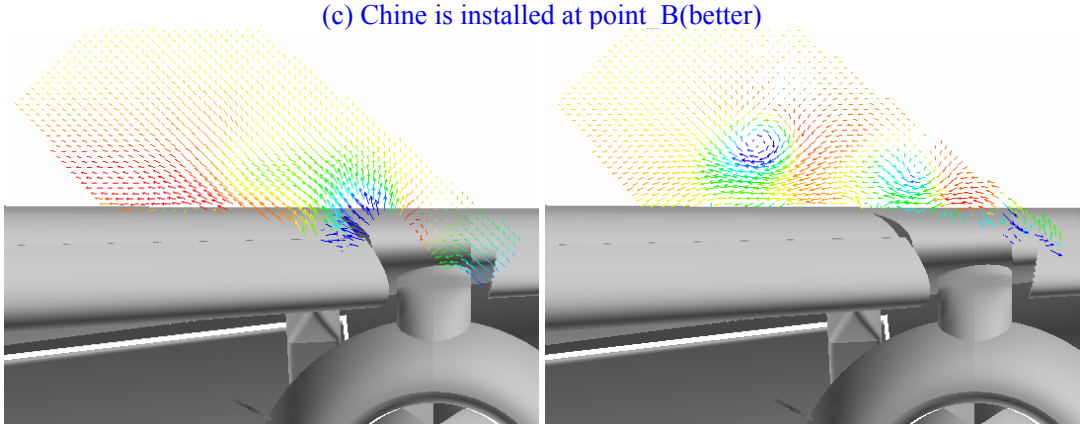

(d) Chine is installed at point_A(reference)

Figure 17. Comparison of the velocity and vorticity magnitude measured by PIV.
(left: first section of Fig.16, right: second section of Fig.16)

In the case where the chine is installed at point_B shown in Fig.17(c), vortices above the pylon and from the chine are visible at the same time. Upward flow near the edge of inner slat seems small though there is the pylon-vortex. This is due to the cancel effect of induced flow by each vortex at that location because they make wall-normal component of the velocity in opposite directions. Therefore, lowspeed region is suppressed near the surface and it doesn't move large in the spanwise direction because the chine-vortex locates comparatively apart from the pylon compared with the case of point_F. In this case, it is considered that the vortex from the pylon is not changed by the chine installation. The influence of the pylon-vortex for aerodynamic performance as described about without the chine case is controlled by the chine-vortex successfully.

Fig.17(d) shows the case of point_A. There is no vortex in the first section, whereas they are clearly shown in the second section. It is considered that when the chine locates at point_A, flow field on nacelle is changed but it never eliminates the vertical structure on the pylon as it is realized by the chine at point_F as shown in Fig.17(b). This flow field delay the generation of two vortices to the downstream of the first section. And, in this case, the mechanism of the flow field structure on the main-wing which is affected by two vortices seems similar to that of point_B shown in Fig.17(c). By the cancel effect of induced wall-normal velocity component between two vortices, lowspeed region is not almost moved upwards. However, it occurs after the mid chord due to the disappearance of the chine-vortex.

Most significant feature of the chine installation effect is categorized into two physics. They are change in original flow field on nacelle/pylon and introduction of the longitudinal vortex from the chine. These effects appear exclusively or bilaterally.

4 Concluding Remarks

In the research program to make aerodynamic design methodology for efficient high-lift system in JAXA, series of lowspeed wind tunnel testing using a realistic aircraft configuration model has been implemented. The interaction between a nacelle/pylon and a wing was intensively assessed for two types of nacelle configurations, namely a long-cowling nacelle and a short-cowling nacelle. As a result, the short-cowling nacelle reduced the unfavorable aerodynamic interaction, and then the stall angle of attack and the maximum lift coefficient increased. Then, aerodynamic performance for the short cowling configuration near maximum lift condition was improved by a kind of vortex generator "chine" installed on the nacelle. In the testing, an efficient design process using Generic Algorism (GA) with Kriging surrogate model was applied in order to explore the optimum location for the chine. Results of PIV measurement have clarified how the chine controls the separated flow field structure near the nacelle/pylon and slat-cutoff region. Most significant feature of the chine installation effect is categorized into two physics. They are change in the original flow field on nacelle/pylon and introduction of the longitudinal vortex from a chine. In our research, characteristics of each effect appeared depending on the chine installation points. However, advantage of each effect should be considered more extensively in other flow conditions and model conditions.

Acknowledgement

We would like to express our appreciation to member of Wind Tunnel Technology Center and Civil Transport Team of JAXA,

References

[1] C. L. Rumsey and S. X. Ying, "Prediction of high lift: review of present CFD capability," Progress in Aerospace Science, Vol.38, 2002, pp. 145-180.

[2] Hansen, H., Thiede, P., Moens, F., Rudnik, R., and Quest, J., "Overview about the European High Lift Research Programme EUROLIFT," 42nd AIAA Aerospace Sciences Meeting and Exhibit, AIAA Paper 2004-0767, Reno, NV, 2004.

[3] Rudnik, R., Germain, E., "Re.-No Scaling Effects on the EUROLIFT High Lift Configurations," 45th AIAA Aerospace Sciences Meeting and Exhibit, AIAA Paper 2007-752, Reno, NV, 2007.

[4] Rudnik, R., Geyr, H., Frhr, v., "The European High Lift Project EUROLIFT II – Objectives, Approach, and Structure," 25th AIAA Applied Aerodynamics Conference, AIAA Paper 2007-4296, Miami, FL, 2007.

[5] Burg, J., W., v., d., Geyr, H., Frhr, v., Heinrich, R., Eliasson, P., Delille, T., Krier, J., "Geometrical Model Installation and Deformation Effects in the European project EUROLIFT II," 25th AIAA Applied Aerodynamics Conference, AIAA Paper 2007-4297, Miami, FL, 2007.

[6] Quix, H., Schulz, M., Quest, J., Rudnik, R., Schröder, A., "Low Speed High Lift Validation Tests Within the EC Project EUROLIFT II," 25th AIAA Applied Aerodynamics Conference, AIAA Paper 2007-4298, Miami, FL, 2007.

[7] Geyr, H., Frhr, v., Schade, N., Burg, J., W., v., d., Eliasson, P. and Esquieu, P., "CFD Prediction of the Maximum Lift Effects on Realistic High Lift Commercial Aircraft Configurations within the European project EUROLIFT II," 25th AIAA Applied Aerodynamics Conference, AIAA Paper 2007-4299, Miami, FL, 2007.

[8] Wild, J., Brezillon, J., Amoignon, O., Quest, J., Moens, F., Quagliarella, D., "Advanced High-Lift Design by Numerical Methods and Wind Tunnel Verification within the European Project EUROLIFT II," 25th AIAA Applied Aerodynamics Conference, AIAA2007-4300, Miami, FL, 2007.

[9] Murayama, M., Lei, Z., Mukai, J., and Yamamoto, K., "CFD Validation for High Lift Devices: Three-Element Airfoil," Proceedings of 2004 KSAS-JSASS Joint Symposium on Aerospace Engineering, Seoul, 2004.

[10] Murayama, M., Yamamoto, K., and Kobayashi, K., "Validation of Computations Around High-Lift Configurations by Structured- and Unstructured-Mesh," Journal of Aircraft, Vol. 43, No. 2, 2006, pp. 395-406.

[11] Ito, T., Yokokawa, Y., Ura, H., Kato, H., Mitsuo, K., and Yamamoto, K., "High-Lift Device Testing in JAXA 6.5M X 5.5M Low-Speed Wind Tunnel," 25th AIAA Aerodynamic Measurement Technology and Ground Testing Conference, AIAA Paper 2006-3643, San Francisco, CA, 2006.

[12] Yokokawa, Y., Murayama, M., Ito T., and Yamamoto, K., "Experiment and CFD of a High-Lift Configuration Civil Transport Aircraft Model," 25th AIAA Aerodynamic Measurement Technology and Ground Testing Conference, AIAA Paper 2006-3452, San Francisco, CA, 2006.

[13] Murayama, M., Yokokawa, Y., Yamamoto, K., Ueda, Y., "CFD Validation Study for a High-Lift Configuration of a Civil Aircraft Model," 25th AIAA Applied Aerodynamics Conference, AIAA Paper2007-3924, Miami, FL, 2007.

[14] Payne, F., M., "Low Speed Wind Tunnel Testing Facility Requirements –A Customer's Perspective," 37th Aerospace Sciences Meeting and Exhibit, AIAA Paper99-0306, Reno, NV, 1999.

[15] Kato, H., Watanabe, S., Murayama, M., Yokokawa Y., and Ito, T., "PIV Investigation of Nacelle Chine Effects on High- Lift System Performance," 48th Aerospace Sciences Meeting and Exhibit, AIAA Paper2008-240, Reno, NV, 2008.

[16] Jewel, B., Barlow, William, H., Rea, Jr., Alan, Pope, Low-Speed Wind Tunnel Testing, 3rd ed., Willy-Interscience, New York, 1999, pp. 367-398.

[17] J., J., Thibert, "The Garteur High Lift Research Programme," AGARD CP-515, pp. 16-1-16-21.

[18] F., M., Payne, "High Reynolds Number Studies of Boeing 777-200 High Lift Configuration in the NASA ARC 12' Pressure Tunnel and NASA LaRC National Transonic Facility," 18th AIAA Applied Aerodynamics Conference and Exhibit, AIAA Paper 2000-4220, Denver, CO, 2000.

[19] Murayama, M., Yokokawa, Y., Yamamoto, K., "Validation study of CFD Analysis for High-Lift Systems," 25th International Council of the Aeronautical Sciences, ICAS-Paper2006-2.3.1, Hamburg, Germany, 2006.

[20] Yokokawa, Y., Murayama, M., Kanazaki, M., Murota, K., Ito T., and Yamamoto, K., "Investigation and Improvement of High-lift Aerodynamic Performances in Lowspeed Wind Tunnel Testing," 48th Aerospace Sciences Meeting and Exhibit, AIAA Paper2008-350, Reno, NV, 2008.

[21] Jeong, S., Murayama, M., and Yamamoto, K., "Efficient Optimization Design Method Using Kriging Model," Journal of Aircraft, Vol. 42, No. 2, 2005, pp. 413-420.

[22] Kanazaki, M., Jeong, S., and Murayama, M., "High-Lift System Optimization Based on Kriging Model Using High Fidelity Flow Solver," Transactions of the Japan Society for Aeronautical and Space Science, Vol. 49, No. 165, 2006. pp. 169-174.

[23] Kanazaki, M., Yokokawa, Y., Murayama M., Ito, T., Jeong, S., Yamamoto, K., "Efficient Design Exploration of Nacelle Chine Installation in Wind Tunnel Testing," 48th Aerospace Sciences Meeting and Exhibit, AIAA Paper 2008-155, Reno, NV, 2008.

Copyright Statement